Making it big : how characean algae use cytoplasmic streaming to enhance transport in giant cells

Meent, J.W. van de

5 MEASUREMENTS OF VACUOLAR FLOW

In this chapter we present measurements of the internodal flow in Chara Corallina making use of two different techniques. Our first set of experiments utilises a method based on Nuclear Magnetic Resonance (NMR), known as Magnetic Resonance Velocimetry. The second makes use of the injection of fluorescent microspheres combined with particle tracking and image velocimetry. The NMR experiments produce highly accurate measurements of the vacuolar flow profile that show excellent agreement with hydrodynamic predictions. The injection based methods are shown to be less effective for the measurement of full cross-sectional profiles, but may be used to obtain localised measurements with high spatial resolution.

The perhaps best known experiments on flow in Chara cells are those of Kamiya and Kuroda (1956), who measured the velocity along 1-dimensional cross-sections in rhizoids, leaf cells and protoplasm-filled internodes. Their technique determined velocities by tracking the time needed for native particles to traverse a fixed distance. Pickard (1972) used a similar method, tracking particles with a range of radial and angular positions, showing that velocities were consistent to experimental precision with his approximated solution for a cell with straight indifferent zones. The most accurate measurements of internodal flows to date are those obtained in the laser Doppler scattering experiments by Mustacich and Ware (1977).

While these measurements are compatible with the simplest hydrodynamic descriptions, no full 2-dimensional measurements of the cross-sectional flow profiles have been presented to date. NMR based techniques are able to improve on existing results allowing a degree of comparison with experiments not previously possible, while tracking based have potential for more accurate localised measurements.

This chapter will begin with a discussion of the Magnetic Resonance Velocimetry and the internodal flow profiles obtained with this technique. We will then continue with an explanation of the injection protocol and compare the results of particle tracking and image velocimetry analysis to the NMR based results. Finally we discuss the utility of the injection method for microrheology and transport experiments.

5.1 Flow Measurements Using Magnetic Resonance Velocimetry

In recent years, measurement techniques based on Nuclear Magnetic Resonance (NMR) have increasingly found use in non-medical applications. The advent of Magnetic Resonance Velocimetry (MRV) has made it possible to perform non-invasive flow measurements on microscopic scales (Elkins and Alley, 2007). The capabilities of MRV have already found application in a range of settings which aid the development and validation of numerical codes or theoretical models; for example, the visualisation of microfluidic flows (Akpa et al., 2007), the imaging of structure and convection in solidifying mushy layers (Aussillous et al., 2006), bifurcation phenomena in the flow through a sudden expansion in a circular pipe (Mullin et al., 2009), and velocity distributions within a three-dimensional vibro-fluidised bed (Huntley et al., 2007). With sufficient time-averaging, spatial resolutions of 10-100 μm can be achieved, allowing imaging of biological systems on scales just slightly larger than those of typical single cells (Choma et al., 2006). While this technique has successfully been applied at tissue level in a variety of plant systems (Scheenen et al., 2001; Kockenberger et al., 2004; Windt et al., 2006), it is in the uniquely sized internodes of *Chara* that we can obtain measurements of flows internal to single cells.

We will begin this section with a basic overview of the underlying physics of Nuclear Magnetic Resonance and techniques for measurements of spin density. We will then proceed to show how these techniques may be used to measure the flow field inside a Characean internode and compare the measured velocity to our hydrodynamic solution. The experiments in this section were performed in collaboration with Andy J. Sederman, who operated the NMR spectrometer and designed the pulse sequences used in the measurements.

5.1.1 An Introduction to Magnetic Resonance Velocimetry

Magnetic Resonance Velocimetry (MRV) is a technique that adapts Magnetic Resonance Imaging (MRI) sequences to measure fluid velocities. MRI methods in turn rely on the principle of Nuclear Magnetic Resonance (NMR) to probe material properties. In order to explain the techniques on which our measurements are based, we begin this section with a brief overview of NMR and the basic techniques employed in MRI and MRV measurements.

Principles of Nuclear Magnetic Resonance

Subatomic particles have the property of spin, which is specified by a quantum number l. Any particle with non-zero spin has a dipole moment associated with it, whose magnitude is governed by a proportionality factor γ known as the *gyromagnetic ratio*,

$$\mu_z = \gamma S_z = \gamma \hbar m \, .$$

Here m is known as the *magnetic quantum number*. This number can take $2l+1$ values, corresponding to dipole moments ranging from $-\gamma\hbar l$ to $\gamma\hbar l$. In the absence of an external magnetic field these $2l+1$ states are degenerate, i.e. their energies are identical. However, the coupling to a magnetic field will induce a small energy difference between the states. This phenomenon is known as the *Zeeman effect*. The energy associated with an external field B_0 (aligned along the z-axis by convention) is given by

$$E_m = -\mu_z B_0 = -\gamma \hbar m B_0$$

The simplest case, and the most common in the context of MRI, is that of spin 1/2 nuclei like Hydrogen, or ^{31}P. These have two eigenstates, often denoted as up (+) and down (-). The corresponding dipole moments of these states are $\mu_z = \gamma\hbar/2$ and $\mu_z = -\gamma\hbar/2$, and the energy difference between the states is therefore given by:

$$\Delta E = \left(E_+ - E_-\right) = -\gamma \hbar B_0$$

The coupling to the magnetic field 'aligns' the spin moments of the nuclei in the sense that nuclei will tend to prefer the lower energy upwards oriented state. More precisely put, the upwards and downwards states correspond to a precession of the spin vector around the z-axis. The rate of precession, which is the same for all states, is known as the *Larmor frequency*, and it is proportional to the gyromagnetic ratio of the particle,

$$\omega_L = -\gamma B_0 \, .$$

Nuclei in the lower energy state can be excited to the higher energy state by absorption of a photon whose energy is equal to ΔE. For a spin 1/2 particle, this energy difference between the states is equal to $-\hbar\omega_L$, so the frequency of this photon needs to be precisely equal to the gyration frequency of the

nucleus. From a spectroscopy point of view this means a magnetised sample will show a resonance peak at the Larmor frequency. This phenomenon is known as *Nuclear Magnetic Resonance*.

In NMR spectroscopy, the rate of absorption is used to probe the properties of a sample. Since the splitting energies are quite low, excitation frequencies lie in the radio part of the electromagnetic spectrum. Because a wide range of materials is transparent to radio waves, NMR spectroscopy can be used to non-ivasively probe objects opaque to frequencies in the visible or infra-red parts of the spectrum. The low energies involved also make the method highly suitable to medical applications.

Since the resonance frequency depends on the strength of the external magnetic field the magnet used is sometimes denoted by the corresponding resonance frequency of a Hydrogen nucleus. For example, in a high-end 21 T magnet protons resonate at a frequency of 900 MHz.

In practice the effective gyromagnetic ratio of a nucleus depends on the chemical environment. The electron configuration in the neighbourhood of the particle will induce a certain degree of diamagnetic shielding, or sometimes de-shielding, thereby altering the resonance frequency. This effect is known as the *chemical shift*. It is typically specified in parts per million (ppm) with respect to the operating frequency of the magnet. Thus, when performing proton NMR spectroscopy an 900 MHz magnet, a chemical shift of 10 ppm would mean a 9 kHz shift in resonance frequency.

Relaxation Processes

In NMR and MRI experiments the sample is excited by an RF-frequency pulse, after which material properties are inferred from the decay of the signal towards the ground state. In most sequences excitation of the sample is achieved through a so-called 90° *pulse*, which rotates the mean magnetisation into the xy-plane. This rotation results from the application of a pulsed magnetic field $\boldsymbol{B}_1$ along one of the axes transverse to the external field $\boldsymbol{B}_0$. The action of the transverse field on the mean magnetisation can be understood by way of a semi-classical description. In the laboratory frame, the inclusion of a transverse pulse along the x-axis produces a Hamiltonian of the form (Callaghan, 1993):

$$H_{\text{lab}} = -\gamma B_0 I_z - 2\gamma B_1 \cos(\omega t) I_x \tag{5.1}$$

This Hamiltonian can be rewritten in the *rotating* frame of the precessing nuclei as:

$$H_{\text{rot}} = -\gamma(B_0 - \omega/\gamma)I_z - \gamma B_1 I_x \tag{5.2}$$

When the frequency ω of the transverse pulse matches the Larmor precession frequency ω_0, the effective external field vanishes, and the remaining component $-\gamma B_1 I_x$ effectively rotates the mean magnetisation of the sample.

There are two types of relaxation that are generally utilised in NMR measurements. The first is the relaxation of the mean magnetisation along the axis of the external field. After rotation by a 90° pulse the magnetisation vector initially lies in the xy-plane and relaxes towards its equilibrium value M_0 over a typical time scale T_1

$$M_z(t) = M_0[1 - \exp(-t/T_1)] \,.$$

The second relaxation process relates to the components of magnetisation in the xy-plane. Analogous to the situation in individual nuclei, the mean magnetisation will precess around the external field with the Larmor frequency. Due to local variations in the Larmor frequency this precession will show dispersion over time, causing a loss of coherence on a time scale T_2, which is generally significantly shorter than T_1. Empirically this decay is described by the relation

$$M_{x,y}(t) = M_{x,y}(0)\exp(-t/T_2) \,.$$

In MRI measurements, the sample is repeatedly exited by a pulse sequence with repetition time T_R, which is of the same order as T_1. Depending on the pulse-sequence used, a signal can either be T_1 weighted or T_2 weighted. One method of obtaining a T_1 weighted signal is the repeated application of a rotating pulse over a repetition time $T_R < T_1$. This will cause a *partial saturation* of the mean magnetisation dependent on the repetition time and rotation angle θ. T_2 effects will cancel out over successive measurements. This produces a signal of the form (Callaghan, 1993)

$$M_z = M_0 \frac{1 - \exp(-T_1/T_R)}{1 - \cos\theta\ \exp(-T_1/T_R)} \,. \tag{5.3}$$

Weighting with T_2 can be attained by application of a *spin-echo* sequence. The decay of T_2 signal is attributable to the fact the nuclei will

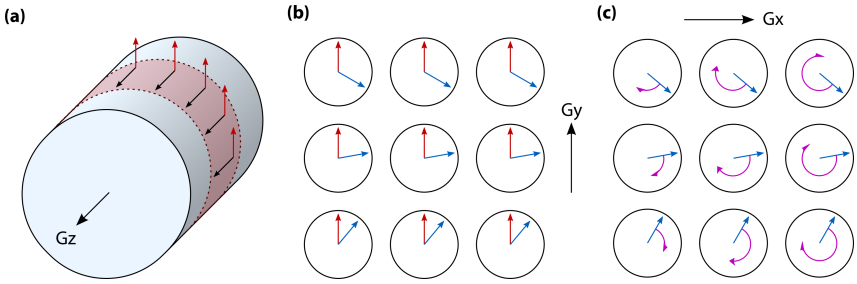

Figure 5.1 Gradient encoding of the position in MRI. **(a)** By application of a secondary gradient G_z during excitation, resonance within the sample is constrained to a *slice* in the xy-plane. **(b)** A brief application of a gradient G_y in between excitation and readout encodes the y-position in a phase shift $k_y \cdot y$ within the sample. **(c)** A third gradient G_x during readout ensures that the frequency of the signal encodes the x-position.

precess at slightly differing Larmor frequencies. A spin-echo sequence flips the xy-components of the spins at an echo time τ. This will place slowly precessing spins ahead of the faster ones, leading to a refocusing of the xy-plane magnetisation as the faster precessing spins catch up at a time τ after the 180° pulse. This phenomenon is known as a *spin echo*. The resulting signal depends on both T_2 and the echo time, and its strength is phenomenologically represented by (Callaghan, 1993)

$$M_{xy}(2\tau) = M_0 e^{-2\tau/T_2}. \tag{5.4}$$

Magnetic Resonance Imaging

The phrase Magnetic Resonance Imaging (MRI) is used to denote techniques that utilise a *pulse-sequence* in which excitation of the sample is followed by a series of phase shifts that allow acquisition of spatially resolved image in Fourier space. A variety of techniques exist for obtaining spatially resolved images, all of which rely on the same basic principles. By application of a series of linear field gradients $\boldsymbol{G}$ to the magnetic field, the Larmor precession rate becomes dependent on the position in the sample:

$$\omega(\boldsymbol{r}) = \gamma \boldsymbol{B}_0 + \gamma \boldsymbol{G} \cdot \boldsymbol{r}\,. \tag{5.5}$$

The brief application of a gradient during the pulse sequence will therefore produce a phase shift $\Delta\phi$ in the sample. This shift will depend on both the

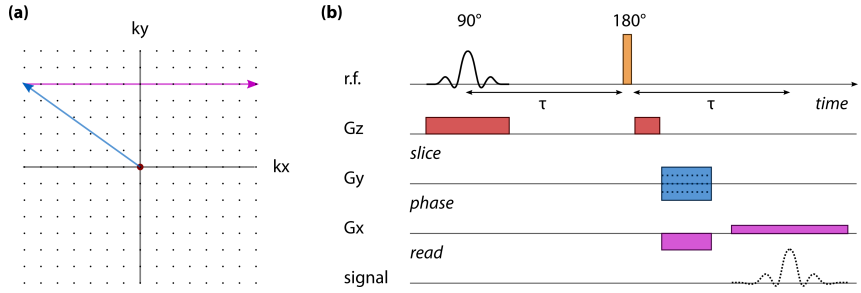

Figure 5.2 Sampling of k-space in a spin-echo sequence. **(a)** The operations in figure 5.1 are equivalent to a shift of the signal in Fourier space. Commonly gradients are applied along both the x and y directions during phase encoding, positioning the sample at $(-k_x, k_y)$. The time-dependence of the signal during readout then allows sampling a full line of points in k_x. **(b)** Schematic representation of a basic spin echo sequence for acquisition of the spin density.

position and the gradient strength:

$$\Delta\phi(\boldsymbol{r}) = \boldsymbol{k}\cdot\boldsymbol{r} \qquad\qquad \boldsymbol{k} = \frac{\gamma}{2\pi}\int \boldsymbol{G}(t')\,dt' \,. \tag{5.6}$$

The amplitude of the signal that is subsequently read out will reflect a local spin density $\rho(\boldsymbol{r})$, averaged over the entire sample. The effect of the gradient field on this signal is that $\rho(\boldsymbol{r})$ will be shifted by a factor $\exp(i\boldsymbol{k}\cdot\boldsymbol{r})$. The volume averaged signal is therefore mathematically equivalent to the Fourier transform of the spin density $\rho(\boldsymbol{r})$:

$$S(\boldsymbol{k}) = \int \rho(\boldsymbol{r}) e^{i\boldsymbol{k}\cdot\boldsymbol{r}}\,d\boldsymbol{r} \,. \tag{5.7}$$

We can thus obtain an image of ρ in Fourier space, or *k-space*, by repeatedly measuring $S(\boldsymbol{k})$ for differing values of $\boldsymbol{k}$. The spin density ρ can subsequently be reconstructed from S by simple application of an inverse Fourier transform. Since $\boldsymbol{k}$ depends only on the integral of $\boldsymbol{G}$ over time, increasing the gradient duration is equivalent to increasing the gradient strength, and these parameters may be used interchangeably to specify $\boldsymbol{k}$.

In a typical imaging sequence (figure 5.2b), a gradient is first used to select a *slice* in the sample (fig 5.1a). This is done by activating a secondary gradient during application of the excitation pulse. Since the Larmor frequency now depends on the position, only the plane in the sample whose Larmor frequency matches that of the excitation pulse will be excited.

The width and shape of this slice can be influenced through the bandwidth and spectrum of the excitation pulse. A *hard* pulse is a broad bandwidth rectangular pulse that is often used to maximise the bandwidth, thereby minimising the time required for the pulse. A pulse of this type will have a long excitation tail away from the centre of the slice due to ringing effects. A Gaussian or sinc shaped *soft* pulse results in a more selective excitation, albeit at the expense of a reduced bandwidth.

Once a slice has been selected, the position within the slice is subsequently determined by the use of two additional techniques known as *phase encoding* and *frequency encoding*. Following the 90° pulse, the magnetisation will precess in the xy-plane. The k_y component to be sample can then be selected by brief application of a G_y gradient. This is called phase encoding (fig 5.1b), because a position-dependent phase shift now tags the position along the y-axis. Finally, a third gradient is applied during measurement so that the frequency of the measured signal becomes dependent on the position along the third axis (fig 5.1c).

In k-space, these operations are equivalent to a shift of the signal $S(\boldsymbol{k})$. The phase encoding applies a single shift k_y, while the frequency encoding is equivalent to a time-dependence in $k_x(t) = \gamma G_x t/2\pi$. A line of points in k-space can therefore be read out by recording the time-dependent signal amplitude during acquisition. In practice, phase encoding is often used along both the x and y axis (fig 5.2a-b). This way, the sample is first positioned at $(-k_x, k_y)$, allowing sampling of the entire interval $[-k_x, k_x]$ during the readout phase, reducing the number of required repetitions.

Figure 5.2b shows a simplified representation of how these techniques are combined in a spin echo pulse sequence. First a 90° slice selection is performed, followed by a 180° pulse to induce a spin echo. A side effect of the slice selection is that the sample has a z-dependent phase shift after excitation, so a second gradient along the z-axis is applied after the 180° pulse to get rid of this unwanted encoding of the z-position. The phase encoding gradients are then applied, after which readout is started to capture the spin echo at time τ after the 180° pulse.

Thus in summary, a selective excitation is used to ensure the first coordinate is known. The k-space in the plane is then sampled by repeating the pulse sequence for different values of k_y, reading out a line of points along k_x each time.

Magnetic Resonance Velocimetry

In Magnetic Resonance Velocimetry, a phase shift is used to measure the velocity of the fluid. The basic principle behind the technique is as follows. First a phase-shift is used to encode the position along the axis of motion. After an time interval Δ, commonly known as the *observation time*, a reverse phase-shift is applied. When the sample is stationary, the net phase shift due to this operation will be zero. However, when movement occurs within the sample, a residual phase-shift proportional to the velocity $\boldsymbol{v}$ can be recovered from the signal.

The principles behind these measurements can be understood as follows. For a fluid element in a flowing sample, the trajectory $\boldsymbol{r}(t)$ may be approximated by

$$\boldsymbol{r}(t) = \boldsymbol{r}_0 + \boldsymbol{v}_0 t + \frac{1}{2}\boldsymbol{a}_0 t^2 + \dots \,, \tag{5.8}$$

where $\boldsymbol{v}_0$ and $\boldsymbol{a}_0$ denote the velocity and acceleration of the fluid element at t=0. Within this moving frame, the phase shift resulting from the application of an additional time-dependent gradient $\boldsymbol{g}(t)$ can then be expressed as

$$\phi(t) = \phi_0 + \gamma \int_0^t \boldsymbol{g}(t') \cdot \boldsymbol{r}(t')\, dt' \,, \tag{5.9}$$

which expands to

$$\begin{aligned} \phi(t) = \phi_0 &+ \boldsymbol{r}_0 \cdot \gamma \int_0^t \boldsymbol{g}(t')\, dt' \\ &+ \boldsymbol{v}_0 \cdot \gamma \int_0^t t' \boldsymbol{g}(t')\, dt' \\ &+ \boldsymbol{a}_0 \cdot \gamma \int_0^t t'^2 \boldsymbol{g}(t')\, dt' \,. \end{aligned} \tag{5.10}$$

If we now define the n-th moment of the gradient as

$$\boldsymbol{g}_n = \int_0^\Delta t^n \boldsymbol{g}(t)\, dt \,, \tag{5.11}$$

then the next phase shift due to $\boldsymbol{g}$ can be written as:

$$\Delta\phi = \gamma \left(\boldsymbol{r}_0 \cdot \boldsymbol{g}_0 + \boldsymbol{v}_0 \cdot \boldsymbol{g}_1 + \tfrac{1}{2}\boldsymbol{a}_0 \cdot \boldsymbol{g}_2 + \dots\right) \tag{5.12}$$

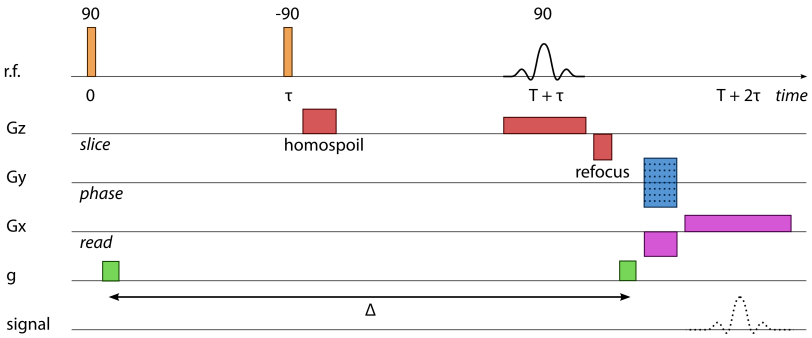

Figure 5.3 Stimulated echo sequence with velocity encoding gradient g, as used in our experiments. A motion encoding gradient is applied immediately after excitation. After a time Δ a reversing pulse is applied, resulting in a phase shift proportional to the displacement over the time interval Δ. In order to maximise the observation time Δ, a *stimulated echo* sequence is used. Here, the magnetisation is 'stored' by using a second 90° pulse to rotate it back along the z-axis. After an interval T, a third pulse is then used to rotate the magnetisation back into the xy-plane, resulting in a 180° flip that induces an echo at time $T + 2\tau$.

An MRI pulse sequence can thus be extended to encode the velocity by inserting a pulse g with zero $\boldsymbol{g}_0$ and $\boldsymbol{g}_2$ moments. The measurement procedure is otherwise unaltered, with the notable exception that the addition of the velocity encoding gradient $\boldsymbol{g}$ now produces a complex spin density $\rho(\boldsymbol{r})\exp(i\,\gamma\,\boldsymbol{v}\cdot\boldsymbol{g}_1)$, allowing reconstruction of the velocity profile from the complex phase of the spin density. Analogous to how the first moment $\boldsymbol{g}_1$ encodes the velocity, the second moment $\boldsymbol{g}_2$ can in principle be used to encode the acceleration $\boldsymbol{a}_0$.

When measuring small velocities, diffusive displacements can dominate over advective flow for short observation times Δ. Since the magnitude of diffusive displacements increases as $\Delta^{1/2}$, while advective transport increases as Δ, the signal to noise ratio of the measurements can be improved by maximising the observation time. For this purpose MRV experiments commonly employ a *stimulated echo sequence* (fig 5.3) to extend the time between excitation and read out. Here, the xy-plane magnetisation is allowed to disperse over a short echo time τ, after which a second 90° pulse is applied, that orients the xy-magnetisation back along the z axis. This 'stores' the dispersion along the z-axis where it is subject to slower T_1 decay, an effect whose explanation requires a quantum mechanical view

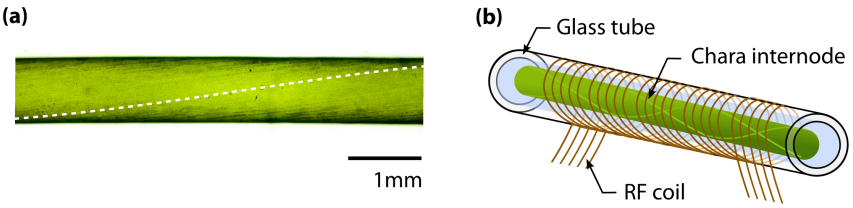

Figure 5.4 (a) Microscopy image of the sample prior to insertion into the glass tube. The dotted line shows a spiral of dimensionless wavelength $\lambda/R = 42$. **(b)** Schematic of sample holder enclosed in a horizontal RF coil. The length of the tube is 40 mm.

that is beyond the scope of this introduction. During this storage, a *homospoil* pulse is used to wipe out any residual coherence in the xy-plane. By application of a third 90° pulse the stored components are now effectively flipped, resulting in a delayed echo at time $T + 2\tau$. It is this type of sequence that we employ in our MRV experiments, where the observation time needs to be as long as possible to increase the ratio of advective motion to diffusion. By careful selection of the magnitude of the applied field gradients and the observation time, this type of pulse sequence allows measurement of velocities from ~10^{-5} – 10 m/s can be measured, depending on fluid properties.

5.1.2 Measurement Protocol

Our experiments were performed on internodes excised from *Chara corallina v. australis* as grown in our lab, originally obtained from the Botanic Garden of the University of Cambridge, courtesy of J. Banfield. The plants were grown in a non-axenic culture, rooted in non-fertilised soil in a 100 litre tank filled with Artificial Pond Water (1 mM NaCl, 0.4 mM KCl, 0.1 mM $CaCl_2$). The tank was kept at room temperature and illuminated with a bench lamp on a 16/8 hour day-night cycle. Once the plants had matured, they were kept at relatively low light levels to prevent lime deposition. During illumination, the light intensity at the top of the tank was ~ 250 lux. Samples of suitable size were placed in a Petri dish under a microscope to verify healthy streaming.

To measure the cross-sectional flow inside the internodal vacuole, a sample was placed in a 1.6 mm inner diameter glass capillary 40 mm in

length, which was pre-filled with Forsberg medium (Forsberg, 1965). The capillary was inserted into a horizontal solenoidal radio-frequency (RF) coil (figure 5.4b). The capillary tube was closed with PDMS plugs and a small volume of silicone grease to ensure a good seal over the measurement time of 192-256 minutes needed to obtain the high resolution measurements.

Note that since our sample is inserted horizontally into the NMR magnet coil, the long axis of the cell lies in the xy-plane of the magnet. The z-axis in these experiments is therefore taken to denote the long axis of the cell, which is also the slicing axis since we are measuring cross-sectional profiles, but is not the same as the orientation of the external magnetic field. The x and y axes still denote the read and phase axes respectively, which are identical to the cellular flow axes used throughout this work.

Velocimetry measurements were obtained using a pulse sequence designed by A.J. Sederman on a Bruker Spectrospin DMX 200, 4.7 T magnet with a 20 mm long solenoid coil of diameter 3 mm. ^{1}H images were acquired at 199.7 MHz. Spatial resolution was achieved using 3-axis shielded gradient coils providing a maximum gradient strength of 49 G cm^{-1} in each direction. Spatial imaging gradients were applied after the motion encoding to minimise diffusive attenuation. Hard 90° RF pulses were used except for the final pulse which was a Gaussian-shaped selective 90° RF pulse 512 μs in duration. Experimental parameters used for the velocity images were: observation time, Δ= 500 ms; velocity gradient duration, d = 1.62 ms; gradient increment, g_{inc} = 10 G cm^{-1}; number of velocity gradient increments, 2; recycle time, TR = 1.9 s; number of scans = 16; field-of-view = 2 mm × 2 mm; pixel array size $N_{\text{read}} \times N_{\text{phase}}$ = 128 × 64; in-plane spatial resolution = 16 μm × 31 μm; slice thickness = 1 mm; measurement duration = 64 min.

For each data set, 4 measurements were taken between 3 and 7 hours apart and subsequently averaged. A Gaussian smoothing with 31 μm Full Width at Half Maximum (FWHM) was selectively applied to the streaming region whilst avoiding blurring at the cell periphery. The streaming velocity in the individual measurements was not observed to vary significantly over the 15 hour period of acquisition. Throughout the measurements the temperature was maintained at 298 K by a regulated airflow system.

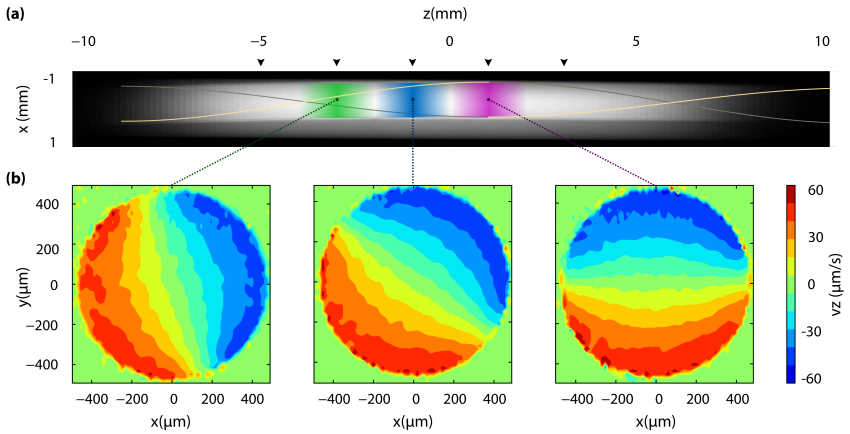

Figure 5.5 MRV measurements of the cross-sectional velocity profiles **(a)** NMR image of the sample, with the measurement volumes at $x = -3$ mm , -1 mm, 1 mm marked in green, blue and magenta. Dotted lines mark the extrapolated position of the indifferent zones, as determined from the orientation of velocity profiles at 5 measurement points between $x = -5$ mm and $x = 3$ mm (marked with black arrowheads). **(b)** Cross-sectional plots of the velocity at each of the marked slices. The resolutions along the $y-$ and $z-$axis are 16 µm and 31 µm respectively.

5.1.3 Results and Comparison to Theory

Figure 5.5a shows an MRI spin density image of the sample, with three slices along the z-axis marked in green blue and magenta. The location of the indifferent zones (dotted lines) was determined by five short measurements taken at positions 2 mm apart (fig 5.5a, arrowheads). The helical pitch is 18.6°/mm, equivalent to a dimensionless wavelength of $\lambda = 42.0$, in good agreement with our estimate from the light-microscopy image in figure 5.4b.

The velocity profiles at each of the slices are shown in figure 5.5b. Due to the usage of a soft pulse during slice selection, the acquired data is averaged along the z-axis with a Gaussian weighting of 1 mm FWHM. This means that the helical axis shifts by about 20° over the averaging volume, producing an apparent 'widening' of the indifferent zones with respect to the theoretical profile. Mean flow velocities are $\sim$ 45 µm/s. These values fall within the range of typical velocities observed in our lab, though the low ambient light levels inside the coil may have reduced the streaming rate somewhat (Plieth and Hansen, 1992).

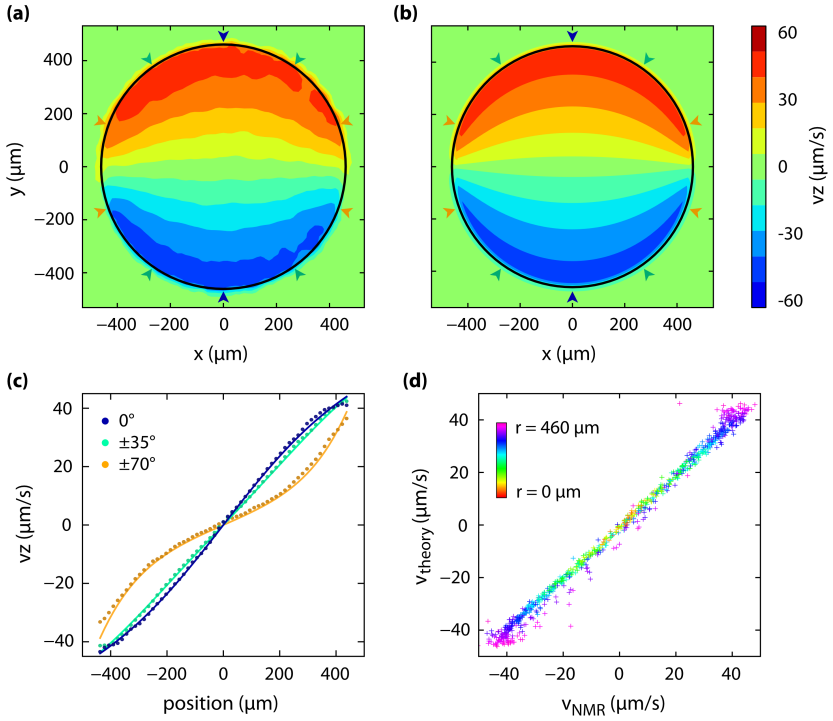

Figure 5.6 Comparison between measurements and theoretical solution. **(a)** Reconstructed profile created by aligning and averaging the data sets shown in figure 5.5*b*. **(b)** Corresponding theoretical profile. **(c)** Three wall-to-wall velocity sections at orientations of 0°, ±35° and ±70° with respect to the $y-$axis (see arrowheads in panels above). **(d)** Comparison between measurements and theoretical values. Data points from all three profiles are shown as markers, with the colour of the marker denoting the radial position of the data. For clarity, only 1 in 10 points is shown.

In order to further enhance the signal to noise ratio of the profile, we align and average the three datasets in figure 5.5b. The resulting cross-section is shown in figure 5.6a along with the corresponding hydrodynamic solution figure 5.6b. We account for the $\sim 20°$ of helical rotation along the measurement volume by averaging the theoretical expression over a length of 3 mm with the same Gaussian weighting as the MRV measurements.

The two profiles show an excellent agreement between measurement and theory. This correspondence is further demonstrated by the wall-to-

wall 1-dimensional profiles shown in figure 5.6c. These profiles show slices at angles of 0°, 35° and 70°, as marked by the arrowheads in figure 5.6a-b. For the rotated profiles, an interpolated rotated dataset was constructed for rotations in both directions and subsequently averaged along both angles of rotation. Markers show the measured values, lines show the theoretical prediction.

In figure 5.6d, measurement points are plotted against their theoretical values, in the manner of earlier velocity measurements (Pickard, 1972). The colour of the points indicates the radial distance from the centre of the cell. We see a remarkably good correspondence throughout the bulk of the cell, with deviations restricted primarily to points within a pixel from the cell wall, where partial-volume effects become significant.

In summary, the results above show that the velocity field within a characean internodes shows an extraordinary agreement with the theoretical predictions in chapter 3. This shows that for the purposes of studying the vacuolar flow, the precise details of the actin-myosin system within the cytoplasm may largely be ignored, since the bulk flow is simply a shear flow with piecewise constant forced velocity at the periphery. By extension this result also shows that that the vacuolar cell sap indeed behaves as a Newtonian fluid.

5.2 Injection Experiments

In the section above we have seen that MRV may be used to obtain exceptionally accurate measurements of the internodal flow profile that show a near perfect correspondence to our hydrodynamic predictions. In order to gain more insight into how these flow profiles might affect transport, we set out to develop injection experiments. By addition of fluorescent particles to the vacuolar fluid, or the cytoplasm, it should in principle be possible to obtain time resolved measurements of more localised flows. This enables a number of experiments not possible with the time-averaging methods that are intrinsic to the MRV technique.

In this section we evaluate the utility of this method for a number of flow and transport experiments. All experiments in this section were performed in conjunction with C.H. Picard, who also helped design the injection protocol. Our initial findings were that injection of tracers into the vacuole can be done reliably, and a sufficient tracer density for PIV measurements may be achieved by this method. While we were able to suc-

cessfully inject particles into the cytoplasmic layer on several occasions, it proved difficult to develop a reliable protocol that still allowed us to achieve a good tracer density. Recent efforts by V. Kantsler to improve the injection system have increased the reliability of the method somewhat, though it remains difficult to determine conclusively whether particles close to the cytoplasmic layer are in fact in the cytoplasm or in the vacuole.

We will begin this section by outlining our injection protocol. We will then show the flow measurements that may be obtained through particle tracking and PIV of injected tracers. Finally we will discuss some of the trials we performed to see if these techniques could used to extend our insight in vacuolar transport and cytoplasmic rheology.

5.2.1 Injection System

A schematic of the injection system used in our experiments is shown in figure 5.7. An internodal cell is placed on an inverted microscope, inside Polydimethylsiloxane (PDMS) sample holder that has a large cover slip as its base. The sample holder contains a window in the centre that allows access to the sample. A glass micropipette, mounted on a motorised micromanipulator is used for injection. Because of the high osmotic pressure inside internodal cells, the cell needs to be bathed in an isotonic medium prior to puncturing of the cell wall. For this purpose, an inlet and outlet tubing are connected to the ends of the cell holder. By use of a peristaltic pump, the medium surrounding the fluid can be changed, thereby allowing us to alter the osmolarity of the medium during an experiment.

The basic injection protocol is as follows. A sample is placed in the holder and positioned for imaging on the microscope. The micropipette is then filled with solution and positioned near the surface of the sample. A high osmolarity medium is then flushed into the sample holder. This induces a gentle osmotic shock causing the cell to slowly lose turgor. Whilst the cell still retains some stiffness, the surface of the wall is punctured with the micropipette. Once it has lost most rigidity the pipette tip is advanced inward. This avoids a back flow upon entering, which tends to jam the pipette tip and can damage the cell by tearing away parts of the cytoplasm. Injection may then be performed over several minutes, after which the pipette is extracted. The osmolarity of the external medium is then reduced slightly to allow the cell to regain some of its turgor. The wound site is allowed to heal for another 30-60 mins, after which the sorbitol solution may be flushed out and replaced with artificial pond water. Because the

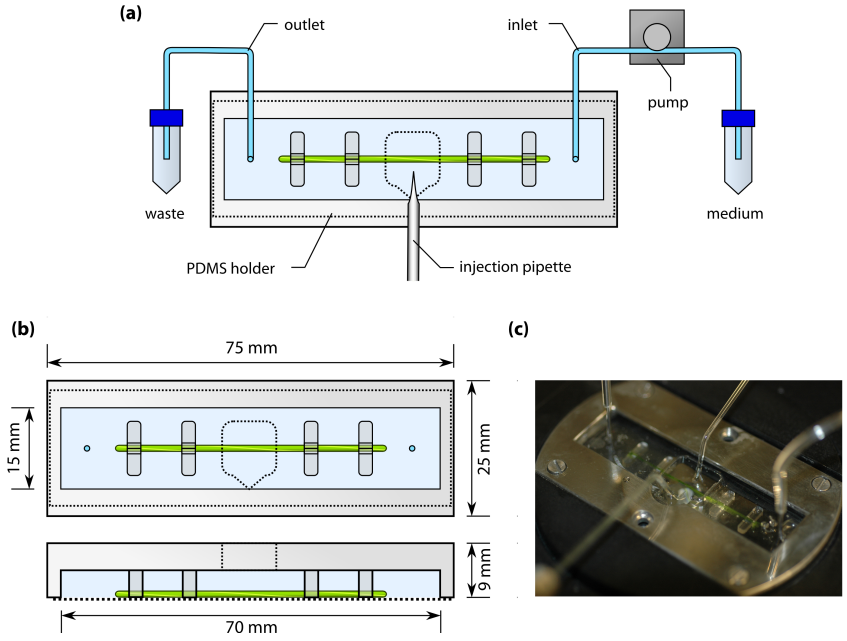

Figure 5.7 (a) Schematic representation of injection setup. The sample is placed in a PDMS holder with a glass coverslip bottom for imaging on a microscope. A window in the top of the sample holder allows access for injection with a micropipette. The cell holder is connected to a changeable medium reservoir to allow the external osmotic pressure to be controlled. **(b)** Dimensions of the PDMS holder **(c)** Photograph of sample holder in stage inset, with positioned micropipette (left) and cell clamp (right).

cell is losing water while it is exposed to a hypertonic medium, relatively large volumes may be injected into the vacuole without over 'inflating' to a point that would cause the site to burst after extraction of the pipette. This allows seeding of the vacuole with a high number of tracers required for PIV, tracking, or transport experiments.

In the next sections we will discuss each of the components in this setup in further detail, after which we will proceed by presenting our measurement results.

Sample holder

Sample holders are created from Polydimethylsiloxane (PDMS), a silicone commonly used as a resin in soft lithography, particularly microfluidics. PDMS is a liquid in its normal form, which can be hardened by treatment with a curing agent, producing an optically transparent rubbery material. PDMS is inert and non-toxic, making it highly suited to biological applications.

The mold for our sample holder was designed and manufactured by D. Page-Croft. Figure 5.7b shows a diagram of the sample holder. The holder is designed to have the dimensions of a standard microscope slide (25 mm × 75 mm) and has interior dimensions of 15 × 70 mm, so that it may be closed off with a large cover glass (22 mm × 74 mm, #391-8055, VWR, Lutterworth UK). Inside the chamber, four wedged clamping posts keep the sample aligned and pressed against the cover glass bottom.

To prevent leakage of medium into the microscope, we use a custom stage inset (fig 5.7c) for our Zeiss Axiovert 200M microscope, also designed and manufactured by D. Page-Croft. This inset uses a clamp that can be tightened by six screws. The base of the inset is lined with a thin rubber gasket to ensure a water tight seal and prevent fracture of the cover slip under pressure. The design also ensures that the PDMS holder is pressed down firmly on the cell minimizing the distance of the sample from the coverslip surface. This is important when imaging the sample with oil immersion objectives, which typically have very short working distances of about 200 μm.

The protocol for production of a sample holder is as follows. About 10 g of Sylgard 184 base elastomer is weighed on a scale (634165S, VWR, UK), after which 10% of curing agent is added by weight. The mixture is stirred 5 minutes and then placed in a vacuum desiccator to degass for about 20 minutes until it is free of bubbles. The PDMS is then poured into the mold which is then placed on a hot plate and cured at 100 C for 10-15 minutes.

Pumping system

In order to allow adjustment of the external osmolarity, a reservoir is connected to each end of the cell holder with Tygon tubing. On the inlet side, the tubing passes through a peristaltic pump (Masterflex C/L 7710-62, Thermo Fisher Scientific, Barrington IL). The outlet side connects to a waste

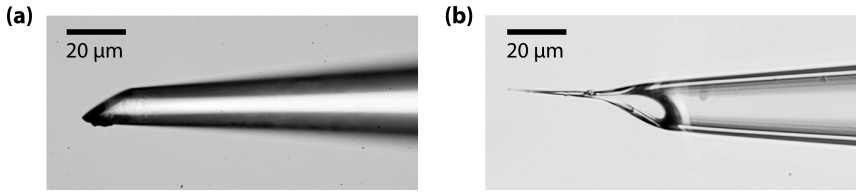

Figure 5.8 Micropipette tips in injection experiments. **(a)** A newly pulled tip is first *bevelled* on a rotating grinding surface, producing a tip with inner diameter of 5 – 10 µm **(b)** The bevelled tip is then *sharpened* on a microforge by briefly letting it touch a glowing filament and then quickly pulling away while the glass cools.

reservoir, whose height can be adjusted to ensure that outflow matches the inflow from the pump. A simple test with cochineal dye showed that the fluid in the cell holder could be exchanged in this manner over a period of 2-3 minutes.

Micropipette fabrication

Micropipette tips used in our experiment are produced in three stages. First a tip is pulled on a horizontal puller (Sutter P-97, Intracel, Royston UK). We use 1.5 mm O.D., 0.86 mm I.D. borosilicate capillaries to increase the rigidity of the tip (#1B150-6, WPI, Stevenage, UK). Since the cell wall in Chara is relatively difficult to puncture, our pulling program is designed to produce a short tip with low flex.

Once tips have been produced, a micropipette beveler is used to create a sloped tip with a smooth surface (Sutter BV-10D, Intracel, Royston, UK). The inner diameter of the beveled tip can be influenced by the bevelling duration (typically about 60 s), as well as coarseness of the grinding surface. Depending on the experiment, the inner diameter of our tips will range from 5 – 50 µm.

Because the tips used in our experiments are relatively large by injection standards, we use a microforge (WPI DMF-1000, WPI, Stevenage UK) to sharpen the protruding edge. In this procedure, the pipette tip is placed on a movable stage on a microscope, and positioned near the surface of a filament under the objective. The filament is then heated running a current through it, causing it to expand slightly. At the point where the expanding filament touches the tip edge, the current is cut and the tip is quickly moved away from the surface of the filament. This results in a sharp tip on

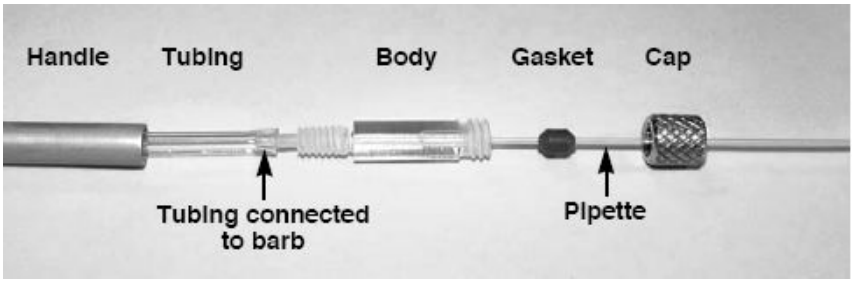

Figure 5.9 WPI PicoNozzle kit for mounting of micropipettes. The pipette is fitted with a rubber gasket and inserted into the plastic body, after which it can be tightened with a metal screw cap. The plastic body is fitted with a male Luer lock barb that connects to the tubing. An aluminium handle is screwed onto the body for mounting on the micromanipulator.

the protruding edge of the pipette, allowing easier puncturing of the cell, while causing less tearing upon insertion.

Pipette loading and mounting

Fluorescent beads and dyes are injected in a buffer of 150-200 mM KCl. Typically, a volume of 100 µl of stock bead concentration was mixed with 1000 µl KCl, resulting a highly concentrated solution containing 0.2% beads by volume. Prior to addition of the fluorescent agent, the KCl buffer is filter sterilised using a 0.26 µm mesh to ensure the buffer is free of particulate matter that could clog the pipette tip.

Pipettes are loaded with injection fluid using the following method. A 1 ml plastic syringe is heated briefly in a Bunsen burner until its tip melts slightly. The tip is then pulled by hand to create a long, thin, flexible nozzle. About 200 µl of injection fluid is loaded into the plastic syringe, which is then inserted all the way into the micropipette to fill it from tip to back. This prevents the formation of an air bubble at the tip.

Our micropipettes are mounted on a motorised 3-axis micromanipulator (Patchstar, Scientifica, Uckfield, UK). In order to ensure a tight seal, a PicoNozzle gasket system (fig 5.9) was used (#5430-15, WPI, Stevenage, UK). Originally, Superthane tubing was used to connect the mounted pipette to a 50 µl airtight syringe (Hamilton, Bonaduz, CH). It was found that the elasticity of the tubing was a limiting factor for control of pressure and flow rates. In later experiments, the Tygon tubing was replaceD by stainless steel, and a smaller syringe of volume 10 µl could be used.

Injection protocol

Our injection protocol is as follows. Once the sample and micropipette have been positioned correctly, we begin by flushing a high osmolarity Sorbitol solution (usually 300 mM) into the sample holder. After a flow period of 60-90 seconds the cell wall is gently punctured. Depending on the observed back flow, the pipette may then be advanced into the cell immediately, or after a short delay. Another 30-90 seconds after insertion of the pipette tip, pressure is applied on the syringe by gently advancing the plunger. In most cases, some cytoplasm will have entered into the pipette tip, resulting in a slight blockage. If too much pressure has to be applied, unblocking of the tip can be abrupt, resulting in excessive flow rates. The stainless steel tubing is an improvement in this regard, allowing a more controlled injection.

After an injection period of 30-300 seconds depending on the experiment, the pressure on the pipette is gently reduced until the flow halts. The pipette is then extracted from the cell. If the osmotic water loss has balanced out the increase of volume from the injection, the wound site should remain closed upon extraction. The external medium can then be replaced with a 200-250 mM solution to prevent further loss of turgor. After another 30-60 min, the concentration may then be reduced further to restore turgor in the cell.

Fluorescence excitation

For imaging of our sample we use a Zeiss Axiovert 200M microscope with motorised z-focus and turret wheel control. The light source used for fluorescence excitation is a X-Cite 120 W Mercury short-arc source (EXFO UK, Hants, UK). A significant issue with fluorescence imaging is that the high light intensity required for excitation can damage the sample. Since chloroplasts have a minimum in their absorption spectrum around 550 nm, we most commonly use a Nile-red fluorescent agent with a 540 nm excitation 600 nm emission filter set (Chroma Technology Corp, Rockingham, VT, US). At low magnification (10x) imaging at this wavelength was found to not significantly damage the sample. At higher magnifications (40x, 63x) some more care must be taken, but measurements over several minutes can still be carried out without damaging the sample in the course of observation.

5.2.2 Velocimetry of Injected Microspheres

In this section we will discuss the flow measurements based on displacements of fluorescent tracer particles. With the widespread adoption of CCD technology, particle tracking and image velocimetry have become standard techniques in research on fluids and soft-condensed matter. Both methods have comparative advantages and remain widely used. Particle Tracking Velocimetry (PTV) is accurate in the sense that velocities are calculated directly from particle positions. Tracking based methods are also suitable for Lagrangian Particle Tracking (LPT) methods, where quantities are evaluated in a Lagrangian set of coordinates. Particle Image Velocimetry (PIV) is computationally robust. Being a method that relies on correlations between small windows in each frame, it can be applied to sequences of images that do not contain well-defined particles, such as the flow of bacterial suspensions (Dombrowski et al., 2004).

Particle tracking methods rely on the identification of tracers in a fluid. Various techniques exist for determination of the particle positions, ranging from weighted averaging of the particle's image, to correlation with a reference and fitting of a Gaussian peak. There are even neural network-based methods that have been shown to be effective for images containing a relatively high degree of noise (Ouellette et al., 2005). Over the past decade these methods have become increasingly sophisticated, and position measurements with errors below 0.1 pixel are now commonly obtained (Crocker and Grier, 1996; Cheezum et al., 2001; Carter et al., 2005; Ouellette et al., 2005). The correct identification of particle correspondences between frames can require some degree of analysis, particularly when displacements between frames exceed the typical particle spacing. Here too various algorithms exist. Typically these analyse the trajectory over several frames to ensure trajectories that are consistent over time (Ouellette et al., 2005).

Particle Image Velocimetry is a technique where displacements are determined by finding the maximum cross-correlation for a shifting interrogation window. Since PIV is a statistical method, its rate of success depends on the number of features in the interrogation image. Keane and Adrian (1992) showed that when performing PIV on a fluid seeded with spot-shaped particles, the success rate shows a well-defined dependence on the number of particles present in both frames. Numbers in the range 7-10 are generally accepted as sufficient for producing accurate results. Due to its statistical nature, PIV is ideally suited for measurements containing high

particle densities, whereas tracking is the more natural solution at lower densities. A great advantage in comparison to tracking based approaches is that PIV can be applied to image sequences lacking well-defined individual particles, as long as the images contain enough features suitable for correlation. Some care should be taken in these cases however, since it can be difficult to obtain an estimate for the equivalent number of 'particles' in the image.

In these experiments we evaluate both PIV and PTV for the measurement of flows in the vacuole and cytoplasm. Our PIV analysis is done using the MatPIV software by Sveen (2004), which allows straightforward computation of PIV velocity fields in Matlab. Typically we use a 64×64 interrogation window and choose our frame interval such that displacements between frames are of order 6-8 pixels to minimize locking effects. Our PTV experiments use custom written software by C.H. Picard.

Comparison of PIV and PTV flow measurements

Figure 5.10 shows a basic cross-sectional flow profile measurement obtained in an injection experiment using 2 μm Nile red beads. After injection, the microscope stage was positioned in the centre of one of the bands and image sequences were acquired at focal distances 20 μm, 200 μm, 300 μm, 400 μm, 500 μm, and 590 μm from the surface of the cell. Acquisition was performed at 10x magnification using a Pike F-145B camera. Images were obtained at 15 fps, with a resolution of 1388×1038, corresponding to a field of view of 1750 μm × 1300 μm. This acquisition rate was chosen to ensure that the typical displacement of particles between two frames would be 2-3 particle distances in the fastest moving regions.

The image sequences obtained from these experiments were subsequently processed with both PIV and PTV to allow comparison of results. A PIV and PTV velocity field in the xz-plane was calculated for each image sequence. Since in-plane velocity variations proved small compared to the accuracy of measurement, velocity components were average over each measurement plane to create two sets of velocity measurements. The resulting profiles are shown in figure 5.10a. The markers show the velocity as determined by PIV (squares) and PTV (triangles). The two methods show good consistency, as should be expected given the averaging over a wide field of view. The measured profiles also show a good correspondence to hydrodynamic predictions.

While it was found that this technique produced reasonable velocity

measurements, initial results showed that image quality was not sufficient to obtain fully resolved 2-dimensional profiles. Since a full view imaging of the cell requires a low magnification, the depth of field of the image can exceed 10 μm. This results in poor resolution along the focus axis, particularly in fluorescence imaging where particles slightly outside the plane of focus will still contribute to the PIV/PTV signal. More importantly, imaging planes near the centre of the cell show a radial drop off in the image intensity, resulting in a 'shadowing' of particles near the edge. This effect is also clearly present in the particle density measurements in section 5.2.4 (see figure 5.12).

As a result of the imaging limitations, the MRV based technique proves more suitable for imaging full 2-dimensional profiles than our injection based method. In particular this means that we were unable to achieve the precision that would be required to measure the secondary components of flow. However the technique shows potential for high resolution imaging with a smaller field of view, as we will show in the next section.

5.2.3 The Flow Profile Near the Tonoplast Interface

One area where higher resolution experiments could yield insights is the details of driving mechanics near the neutral line. These dynamics are determined by a large number of factors that remain largely unknown. First there is the effective force-velocity relationship that results from the collective action of the myosin motors on the cytoplasm. Second is the topology of the actin network, which is known to show a gap near the indifferent zone Wasteneys et al. (1996). Thirdly, the rheology of the cytoplasm remains poorly understood. The best measurements currently available show that it is non-Newtonian showing a power-law dependence $\tau \sim \dot{\gamma}^{1/n}$ in the stress-strain relation with exponent $n = 3$ (Donaldson, 1972). Finally, there is the question how shear is transferred from the cytoplasm to the vacuole. Presumably the tonoplast moves with the cytoplasmic layer and the velocity field is continuous across the tonoplast boundary. If this is indeed the case, it would imply that the tonoplast membrane can robustly support the high rates shear near the indifferent zone. As such, the tonoplast in Characean cells may not only be the largest vesicle known in nature, but also an interesting example of how these membranes can flow under shear.

Due to the complexity of all these interacting aspects, it is clear that understanding the shape of the shear profile near the indifferent zone will

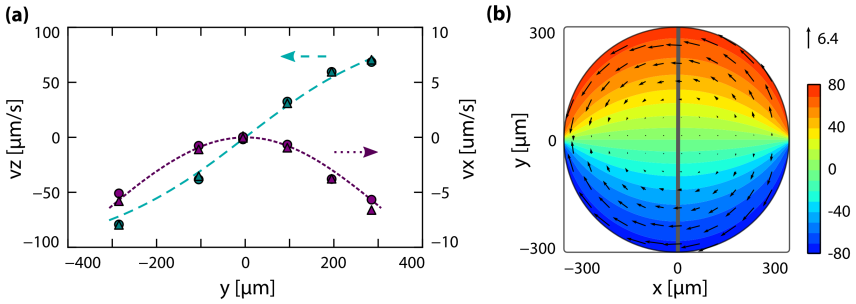

Figure 5.10 Flow profiles obtained with PIV and PTV. **(a)** z-component (cyan) and x-component (magenta) along a slice at x=0. Markers show velocities obtained from PIV (squares) and PTV (triangles), with lines showing the corresponding theoretical profile. **(b)** Corresponding theoretical profile showing the slice position in dark grey.

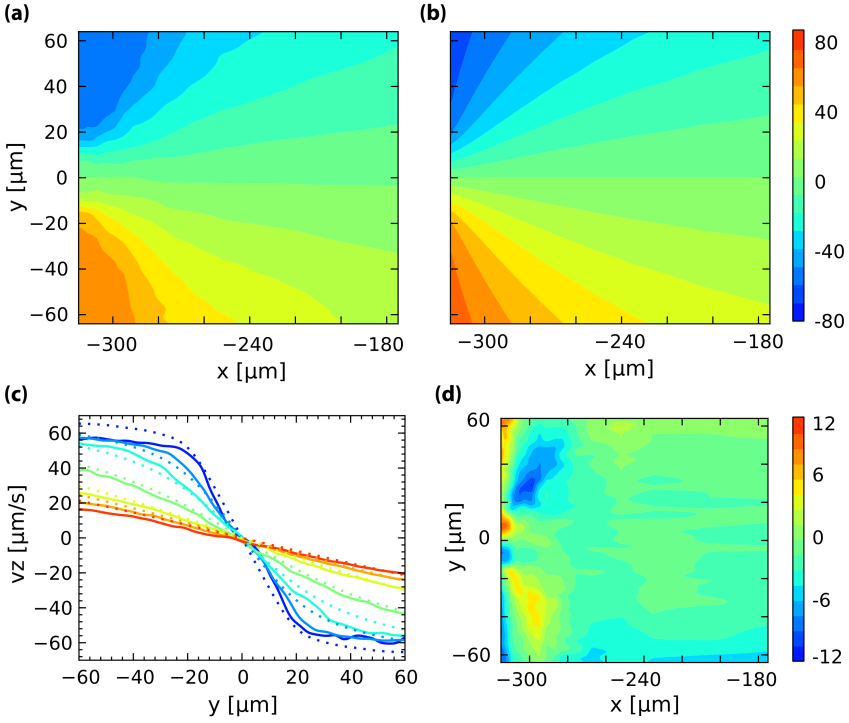

Figure 5.11 Tracking based flow measurements of the shear profile near the indifferent zone. **(a)** Measured flow profile **(b)** Fitted profile with a streaming rate of V = 67 µm/s and linear cross-over at the indifferent zone of width ε = 19 µm. **(c)** Comparison of measurement profiles (solid) to fit (dotted) at x positions −315 µm, −305 µm, −295 µm, −275 µm, −235 µm, −205 µm and −175 µm. **(d)** Difference between measured profile and fit.

require more information than can be obtained from flow measurements alone. However a precise determination of the flow profile certainly offers a good starting point for further analysis. Figure 5.11 shows flow profiles obtained from an experiment performed by V. Kantsler. With the improved control resulting from the use of stainless steel tubing, he was able to seed both cytoplasm and vacuole with 0.5 μm Nile red particles. For imaging, a 63x water immersion objective was used (441470-9900, Carl Zeiss, Welwyn Garden City, UK). This objective combines a relatively high numerical aperture of 1.0 with a long working distance of 2.1 mm, allowing accurate imaging with a field of view of about 240 μm × 120 μm. Image sequences were acquired at focal distances 5 μm, 13 μm, 17 μm, 21 μm, 29 μm, 37 μm, 53 μm, 85 μm, 145 μm with respect to the ectoplasm-endoplasm interface. The radius of the cell was 320 μm and the dimensionless wavelength was $\lambda = 24$.

Particle tracks were obtained from each of the image sequences. Because the presence of chloroplasts distorts particle images, the length the tracks that could be obtained was highly variable, ranging from 3 to 50 frames per particle. Because of this we use a coarse-graining based method to create an averaged velocity profile from these measurements. For each of the particle tracks, the r and ϕ coordinates were determined for each time point, as well as the z-displacement between frames. This resulted in roughly $2 \cdot 10^4$ data points for each image sequence. Each displacement was then multiplied by a radial basis function Φ of Gaussian shape to allow evaluation of the velocity on a grid. The velocity field can thus be calculated from the vectors $(r_i, \varphi_i, dz_i, dt_i)$ using a form of weighted averaging:

$$v_z(r, \phi) = \frac{\sum_i \Phi(|\boldsymbol{x} - \boldsymbol{x}_i| / \sigma) dz_i / dt_i}{\sum_i \Phi(|\boldsymbol{x} - \boldsymbol{x}_i| / \sigma)} \,. \tag{5.13}$$

Here $|\boldsymbol{x} - \boldsymbol{x}_i|$ denotes the distance of the grid point where the velocity is evaluated to the i-th data point. The parameter σ, which is known as the *coarse-graining length*, determines the size of averaging volume around each grid point.

The method outlined above may thus be used to average the velocity data in a helical frame and collapse it to a single profile in the $r\varphi$-plane at $z = 0$. Because of the large number of data points in each imaging plane, an anisotropic coarse-graining length (σ_x, σ_y) was employed to increase resolution along the y-axis of the imaging plane. Grid-points along the y-axis were spaced 0.64 μm apart, and an averaging length σ_y was 2.56 μm.

Along the x-axis, σ_x was taken equal to the distance between neighbouring planes.

The reconstructed velocity profile resulting from this analysis is shown in figure 5.11a. This profile was fitted to a theoretical profile to determine the streaming rate V and indifferent zone cross-over width ε. Two types of boundary velocity functions were tried. First we used a smoothed $\tanh((\varphi-\varphi_0)/\varepsilon)$ dependence as used in other analysis. We found that a somewhat better fit resulted when the tanh dependence was replaced by a linear cross-over of the form:

$$v_b(\varphi) = \begin{cases} V(\varphi-\varphi_0)/\varepsilon & |\varphi-\varphi_0| < \varepsilon \\ V\,\mathrm{sign}(\varphi-\varphi_0) & |\varphi-\varphi_0| \geq \varepsilon \end{cases} \tag{5.14}$$

The fit of the profile is shown in figure 5.11b. As in the MRV measurements, the overall features look very similar. However, closer inspection of the profiles near the wall shows clear qualitative differences. The measurements appear to show a 'dead zone' in between the flowing bands, and the velocity does not decrease as steeply moving inward as it does in the theoretical profile. We also see see that the curvature of the outermost contour lines differs significantly. Figures 5.11c-d show a comparison of the two profiles. Because the velocity gradients are less steep in the measurement data, the theoretical profile overfits the points near the wall, while showing a slight underfit towards towards the centre.

These results appear to show that the presence of the cytoplasm affects the shape of the flow profile in a significant way. Regardless of the details of driving mechanics, a system that is Newtonian should be fully determined by the velocity at the boundary. Our MRV measurements show that this is indeed a very good approximation for the vacuolar flow further away from the walls, but these measurements near the wall show a flow profile that is incompatible with a Newtonian description. The outermost contours show very little shear gradient, which could mean that these regions are flowing cytoplasm that undergo little deformation as they move along the wall. Indeed this would be a detailed confirmation of the sliding theory proposed by Kamiya and Kuroda (1956), which states that the cytoplasm *slides* along the cell wall as a gellified layer.

Certainly we see that these types of experiments show potential for more details studies into the interaction of myosin driving, cytoplasmic rheology and flow. A number of experiments could further elucidate the behaviour of the flow near the cytoplasm-vacuole interface.

Chiefly, it is important to locate the position of the tonoplast in these measurements. We have in tried several methods for visualising the tonoplast. One of the most well known of these is injection of FM1-43, a styryl dye which localises to membranes. While it is straightforward to add this dye to the injection buffer, our finding was that the resulting fluorescence signal was not sufficient identify the position of the tonoplast. Glass beads are known to stick to membranes, but our experience was that adhesion was not strong enough to allow clear identification of the tonoplast position. We also tried coating beads with polylysine, but observed little effect. Another approach may be to attempt two injections using beads with different dyes for the cytoplasm and vacuole. In order to achieve this, our injection protocol would still need some improvement however, since we are currently not able to reliably inject selectively into the cytoplasm.

Another source of information could be the visualisation of the actin network. It is known that FITC-phalloidin can be used for in vivo labelling of actin in characean cells (Wasteneys et al., 1996). If an image of the actin network could be obtained in with a measurement of the flow field, a compelling level of information becomes available that could make it possibly to test theories about myosin driving mechanics and cytoplasmic rheology.

5.2.4 Other Experimental Trials

In the last section we showed that injection of tracer particles allows high resolution and accurate flow measurements at microscopic resolutions. In developing these protocols we envisioned a number of other experiments, which we will discuss briefly in the remainder of this chapter.

Microrheology of vacuolar fluid and cytoplasm

As can be seen in section 2.3.7, relatively little is known about the rheology of internodal cytoplasm and the vacuolar fluid. We have performed simple experiments to see if better information could be obtained by imaging injected particles with a high speed camera. Through the statistical analysis of the particle fluctuations, a technique known as *microrheology*, it is in principle possible to obtain an estimate of the frequency-dependent viscous and elastic moduli.

Our measurements of the vacuolar rheology showed that the viscosity of the vacuolar fluid was indiscernible from water to experimental pre-

cision. Determination of the cytoplasmic rheology was complicated by a number of factors. First among these was the difficulty of achieving reliable injection. In order to image particles in the cytoplasm with sufficient precision, a chloroplast-free window must first be created by exposure of the surface with a bright light source. This causes chloroplasts to swell and detach over a period of about 6-8 hours. Injection can only be attempted afterwards and was initially found to have a low success rate. Our protocol for cytoplasmic injection has somewhat improved recently, so this problem could be resolved in future experiments, though it is not yet clear if a sufficient tracer density can be achieved to allow statistically sound measurements.

A second problem was the reliable suspension of streaming. We halted streaming by application of a modest voltage of 10-15 V across the cell with an external power source, thereby triggering an action potential. While this method successfully suspended streaming for a period of several second, close inspection of the particle data revealed a continuous residual drift in the particle positions. Mechanical stimulation can result in cessation of streaming over a longer period of time, but we were not able to find a method of mechanical stimulation that produced reliable action potentials whilst avoiding wider damage to the cell.

While we suspended our efforts to determine rheology in this manner after initial trials, it may well be worth revisiting this experiment at a later stage. Imaging quality has improved with the installation of the 63x water immersion objective, and injection into the cytoplasm has become easier after injection control was improved with stainless steel tubing. The fact that a chloroplast window must be created means that the number of experiments it will be difficult to obtain large numbers of datasets, but a basic determination of cytoplasmic rheology should be possible in future experiments.

Spreading of tracer particles in the vacuole

Our hydrodynamic description in chapter 3 reveals that the helical nature of the internodal flow implies a small transverse circulation, that is shown to enhance diffusive exchange between vacuole and the cytoplasm in chapter 4. An unanswered question is how spreading along the long axis of the cell is affected by this circulation component. We attempted two experiments to characterise these effects.

In the first experiment, we injected 2 μm Nile red tracers near one end-

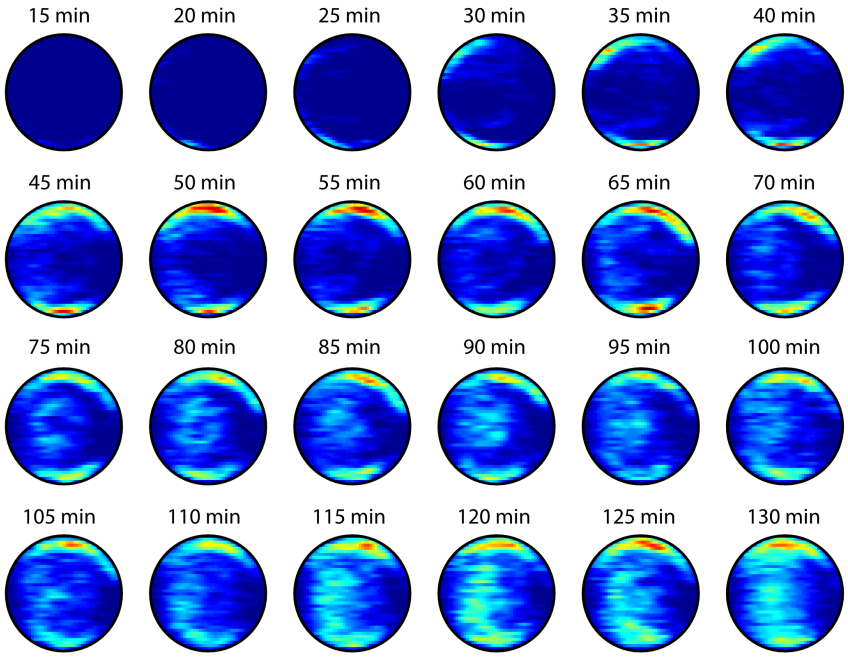

Figure 5.12 Results from a tracer transport experiment. Particles are injected at the end of an internode at t=0. A stack of images is then acquired at intervals of 5 min to obtain the time dependent density upstream from the injection point.

point of an internode. Streaming was inhibited during the injection phase of the experiment by placing an icepack on the microscope stage, thereby lowering the temperature and reducing streaming to negligible rates (see section 2.3.3). The microscope stage was then positioned to image a point upstream in the cell. The motorised z-focus was then used to acquire a stack of images at regular intervals, allowing us to determine the evolution of the upstream density profile with time.

A sample set of acquired density profiles is shown in figure 5.12. Since diffusive spreading of 2 μm tracers is negligible on the time scale of the experiment, the observed changes in concentration are purely the result of advection. We first observe an increase in concentration near the bottom band. 10 minutes later we start to observe particles in the other band as well, which have presumably been transported to the end of the cell, and are now being advected back to the injection point. After about 40 min we start to see a slow increase in the concentration in the centre of the cell.

While the initial results in trials with this technique were reasonable,

the protocol proved unsuitable for quantitative measurements. The chilling technique was successful in inhibiting streaming, we found that temperature control was a limiting factor in these experiments. Excessive chilling appeared to result in a temperature shock that prevented recovery of streaming rates prior to the experiment. Another limitation, as in our initial PIV/PTV flow measurements, is the shadowing near the sides of the cell. Here the sloped cell wall obscures the view and as a result we see an artificial drop off in the apparent density, since particles are not picked up by the image processing routines. Finally, the initial cloud of injected particles was found to not be sufficiently homogeneous to result in reproducible measurements.

In order to find a more reliable method for creating the initial condition in this experiment, we used diamagnetic fluorescent particles (ME03F-/8901, Bangs Laboratories Inc, Fishers IN). By placing a small rare earth metal (NdFeb) magnet on the sample holder the particles could be collected at one endpoint of the cell. In principle, this method has the great advantage that it allows multiple experiments to be run within a single cell. However it was found that while a magnet was effective in capturing the particles, a residual magnetisation would be persist after release, causing particles to be aggregated clumps whose dissociation rates were too variable to allow consistent measurements.

Summary

With the measurements in this chapter we have, for the first time, presented flow profiles with a level of accuracy that allows detailed comparison with hydrodynamic theory. The MRV technique produces full 2-dimensional cross-sectional profiles that show very close agreement the Newtonian shear flow solved in chapter 3. The more localised measurements that were performed using particle tracking techniques reveal a non-Newtonian behaviour near the wall that we hypothesise results from rheological characteristics of the cytoplasmic layer. If these measurements can be extended to obtain information of the underlying actin network, as well as the position of the tonoplast interface, they could provide a level of information that allows testing of theories on myosin driving dynamics, the rheology of the cytoplasm, and the transfer of shear into the vacuole across the tonoplast membrane.